Experimental Mechanics manuscript No.
(will be inserted by the editor)

High-speed, 3D volumetric displacement and strain mapping in soft materials using Light Field Microscopy

S. Buyukozturk[1,2,*] · A. K. Landauer [3,*] · L. A. Summey[1] · A. N. Chukwu[1] · J. Zhang[1] · C. Franck [1‡]

Received: date / Accepted: date

Abstract

Background: High strain-rate deformations of soft materials occur in many applications, and thus measurements of at-rate volumetric deformations are needed to understand physical processes relevant to, for example, hydrogel mechanics or injury biomechanics. Experimentally obtaining volumetric information and applying these techniques at high rates remains a significant challenge, especially at small, micrometer length scales.
Methods: To conduct 3D volumetric imaging at high rates, 100 frames per second (fps) to 10 kfps, we designed a full-field volumetric light field microscopy system paired with a high speed camera and custom particle tracking algorithm. Light field microscopy uses limited-angle tomographic volume reconstruction to obtain fully 3D data from a single 2D image. Simulated and experimental light-field images of particles at assorted strain-rates or frame-rates were created and used as verification and validation. These were used to investigate the sensitivity of the measurement technique to noise and obtain baseline displacement and strain uncertainty bounds for various motion fields. Reconstructed volumes from light field images were post-processed with volumetric particle tracking to quantify 3D volumetric deformations. As an experimental test case a transparent hydrogel seeded with fluorescent particles was deformed in a stage-top device. This custom-built device was programmed to deformed the specimen in nominally simple shear at applied strain rates between $2\,s^{-1}$ and $40\,s^{-1}$, while light-field images were collected at between 500 fps and 2000 fps.
Results: The synthetic and experimental images were used to compare known and reconstructed deformations. This showed that the acceptable imaging signal to noise ratio floor is approximately 10:1, which occurs at around 4000 fps as configured. Rigid body displacements up to $40\,\mu$m in-plane and $400\,\mu$m out-of-plane were tracked with standard errors less than approximately $\pm 1.0\,\mu$m and $\pm 3.0\,\mu$m, respectively. Synthetic large-motion uniaxial tension, rotation, and shear tests demonstrated total mean error less than 3 % engineering strain. The stage-top impact device demonstration showed that the *in-vitro* simple shear impact device applied a uniform strain to the specimen, while revealing a small amount of overshoot error and misalignment, demonstrating the diagnostic capability of HR-VPTM for device calibration experiments.
Conclusion: We demonstrate a full-field volumetric light-field microscopy system paired with post-processing and particle tracking to quantify volumetric displacement and strain fields in soft, transparent materials undergoing high rate deformations.

Keywords Light Field Microscopy · High speed imaging · Particle tracking · 3D deformations

1 Introduction

Volumetric measurement of dynamically deforming materials is a challenge. For low rates, well established techniques may readily be employed. These include, for example, x-ray micro-computed tomography [1], magnetic resonance imaging [2] or optical coherence tomography [3] for optically opaque or semitransparent materials, or, for transparent media, confocal [4], multiphoton [5] or light-sheet microscopy [6]. However, inter-frame acquisition times are usually long compared to the millisecond time scales of the dynamic deformations (e.g., due to the

[1]Department of Mechanical Engineering, University of Wisconsin-Madison, Madison, WI, USA 53706
[2]School of Engineering, Brown University, Providence, RI, USA, 02912
[3]Material Measurement Laboratory, National Institute of Standards and Technology, Gaithersburg, MD, USA, 20899
[*]Contributed equally [‡]E-mail: cfranck@wisc.edu

sequential nature of scanning or rastering), posing significant challenges for obtaining dynamic volumetric motion information [7,8]. Relatively planar imaging and localization techniques, such as aberration-based methods [9], 2.5D microscopy [10], or diffractive optics-based methods [11,12], show great promise for high-rate measurement with exceptional localization performance. However, aspect ratios of lateral to vertical are typically on the order of 10:1, e.g., 9 slices at 2 μm spacing [12] or 25 slices at 250 nm [11], and capturing equiaxed volumes for fully 3D dynamic events remains elusive. Thus, despite a demonstrated need for high-rate equiaxed volumetric deformation measurement, for example to study traumatic brain injury [13,14], it has been a challenging barrier to overcome. In parallel with diffractive techniques, light field microscopy (LFM) has been developed as a similar technique capable of reconstructing nearly equiaxed volumetric data from single 2D images, allowing practitioners to utilize the full framing rate of a standard high-speed camera for each volume image at the cost of photon efficiency and some of the native resolution of the microscope [15,16,8,12]. The 3D information in LFM is achieved by structuring the light via a microlens array placed at an intermediate imaging plane and employing the principles of limited-angle tomographic volume reconstruction using the resultant parallax from individual perspective views [17, 18], making LFM a type of multi-perspective tomographic imaging. In scene-scale imaging, similar light-field techniques are referred to as integral imaging or plenoptic imaging, and enable computational refocusing and depth reconstruction [18,19,20,21], whereas LFM has largely involved volume reconstruction [16,22,23,17]. LFM has most widely been applied in biological applications, for example in volume imaging of neuronal activity [22,16, 24,25] or perspective viewing of *C. elegans* [26].

Multi-perspective tomographic imaging for motion tracking has predominately been advanced to study fluid dynamics and has been combined with particle image velocimetry (PIV) or particle tracking velocimetry (PTV) by utilizing fluorescent tracer particles [27,28] as fiducials. Camera arrays are often employed to achieve parallax for multi-perspective imaging rather than a microlens array, e.g., TomoPIV-based techniques [29,30,28]. In microfluidics, however, microlens-based LFM has been demonstrated as a tool for flow characterization with fluorescent micro-particles and PIV [31,32], but is typically limited to standard scientific cameras at relatively low rates less than 500 frames per second (fps). An implementation of LFM using an additional diffraction grating has recently been demonstrated with moderate rate imaging (tens of fps to hundreds of fps) for digital volume correlation (DVC) [33]. However, LFM-based motion tracking has remained largely unused for volumetric deformation measurement in rapidly deforming soft solids, especially at imaging rates greater than approximately 200 fps.

Deformations during dynamic events on time-scales of milliseconds or microseconds have typically been approached by assumptions of symmetry [34] with slice- or point-based deformation inputs to fully 3D models [35, 36]. Whereas, when using LFM, the same high-speed camera previously employed for single-slice imaging may now be used to generate volumetric displacement and strain fields. Typically volumetric motion reconstruction uses either correlative methods [37], e.g., digital volume correlation [38] or particle image velocimetry [29], or particle tracking techniques [27,39,28]. Correlative techniques typically require high-density particles, which are incompatible with LFM reconstruction, and act as smoothing filters on the recovered displacements [38,37]. In contrast, particle tracking techniques can provide high accuracy and robust motion reconstruction for widely varying particle densities and displacement spatial frequencies [39,28], but recovering dense, Eulerean-frame displacement and strain fields from sparse tracking data is an additional challenge, e.g., as discussed in Hazlett *et al*. [40] and Yang *et al*. [41].

In the present work, we describe a new implementation of a light-field system integrated into a microscope base with supporting light-field volume reconstruction and particle tracking-based displacement and strain field measurement tools, which we name High Rate Volumetric Particle Tracking Microscopy (HR-VPTM), which we validate using known synthetic and experimental displacement fields. We discuss its application for deformation measurement with a new device designed to impose a simple shear strain impulse with controlled amplitude and frequency to *in-vitro* neural cultures [42]. These tools are directly applicable to small-scale deformation tracking of dynamic volumetric events in optically transparent media with fluorescent particles, and may straightforwardly be adapted to any situation where light-field imaging (i.e., plenoptic or integral image) can be used in conjunction with fiducial markers without requiring additional optics.

The remainder of the paper is structured as follows: first, we give an overview of the LFM theory including synthetic LFM image generation and describe our general workflow; second, we outline our systematic evaluation of the the effect of variable experimental conditions (e.g., sensor noise floor, image resolution, dynamic range) on particle tracking uncertainty; third, we detail the specific experimental set up and protocol, including optical configuration, shear device, and image reconstruction and motion tracking algorithms; fourth, we discuss the results from a series of rigid body motion and shear experiments; fifth, and finally, we mention limitations of our current system and provide an outlook for future work.

2 Background

2.1 LFM system and volume reconstruction limitations

The core innovation of LFM is to place an array consisting of many small, approximately 100 μm lenslets, called microlenses, in a microlens array, at the conjugate image plane of a microscopy system. Each lenslet in the array provides a slightly angled perspective, generating small-angle parallax [15,18,20,8]. Using limited-angle tomography via deconvolution, this multi-perspective view produces a comparatively high resolution volume reconstruction [17,43]. An image of a microlens array with a square grid of lenslets is shown in a inset to Fig. 1b, where each lenslet gives a perspective view of the object - in this case a uniformly fluorescent slide. To describe the optical transfer function of the microlens array, fundamental parameters include: the lenslet pitch (the size, or pitch, of an individual lenslet), p_l; the lenslet pixel pitch (pixels per lenslet diameter on the camera sensor), p_p; the microlens focal length, f_l; and the numerical aperture (NA) of the lenslets in the microlens array. The NA of microlens array must match the NA of the imaging microscope objective to ensure that the microlens image behind each lenslet fills the camera sensor plane without overlapping or missing perspective views [15,17].

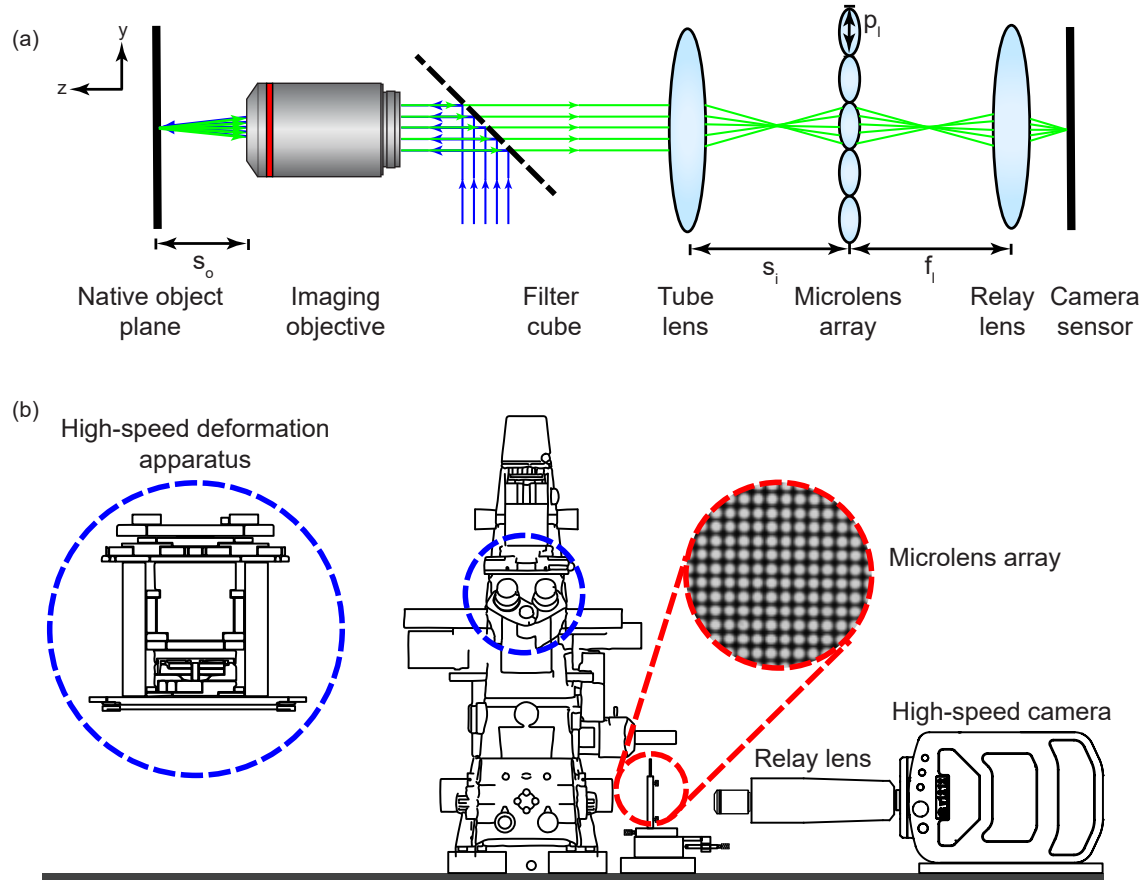

Fig. 1 Light field microscope (LFM) setup for a high-speed application. (a) Illustration of the light path for the setup, showing paths of excitation light (blue) propagating into the sample and emitted light (green) propagating out of the sample, through the LFM optics and to the camera sensor. In this representation of the light path, the system is focused to a point at the native object plane with an in-plane position that results in light rays filling an entire lenslet. (b) Schematic of the inverted microscope with microlens array and high-speed camera as configured for light field microscopy. *Inset, left* Schematic of a given high-speed deformation apparatus designed to operate stage-top with fluorescent microscopy (not to scale). *Inset, right* Snapshot of a uniformly illuminated fluorescent slide propagating through the microlens array

Unlike in traditional microscopy, where the point spread function (PSF) is an invariant of the system, a light-field PSF varies depending on the position of a given point-source. To reconstruct light-field images into volumes, a synthetic PSF of the optical system is cast as a transfer function, $\mathcal{H}$. Given the ground truth volume, $\mathbf{g}$, the light-field, $\mathbf{f}$, is given by the operation of the optical transfer function on the ground truth volume, i.e.,

$$\mathbf{f} = \mathcal{H}\mathbf{g} \tag{1}$$

To solve for the volume $\mathbf{g}$ given the measured light field $\mathbf{f}$, the PSF of optical system $\mathcal{H}$ must be inverted. The widely used Lucy-Richardson-type framework for deconvolution provides an estimate of this inversion by iteratively solving a maximum likelihood estimator formulation [17,22,43]. In the LFM reconstruction, there is a trade off between lateral and axial resolution [8] – this is intuitive from the form of Eq. 1 where the size and dimensionality of the matrices must match for the solution to be well-posed. The spatial resolution depends on the number of lenslets within the field of view, while angular resolution, or depth of field, depends on the number of pixels behind each lenslet. The loss of lateral resolution is proportional to the number of discrete angular samples collected [15]. The lateral aliasing limit is effectively defined as the lenslet pitch divided by the magnification. The angular depth is defined as the number of resolvable spots behind a lenslet, which is a function of the microlens dimensions and diffraction limited spot of the microscope objective. A more detailed explanation of the lateral and axial limitations are available in the seminal work of Levoy *et al*. [15]. To overcome these resolution limits, more recent algorithms introduce depth-dependent and aliasing-aware deconvolution, which provides more flexibility in designing light-field systems [17,43]. By incorporating this deconvolution, the algorithms of Broxton *et al*. [17] and Stefanoiu *et al*. [43] improve reconstruction quality beyond the aliasing limits of direct inversion of $\mathcal{H}$. Using this method, Stefanoiu *et al*. showed that the sub-lenslet lateral and axial resolution increases with increasing distance, z, away from the native focal plane and then gradually falls off once maximum total depth-of-field for the primary objective is reached. Using geometric optics Broxton *et al*. derived the functional form:

$$v_{lf}(z) = \frac{p_l}{0.94\lambda M|z|} \tag{2}$$

where v_{lf} is the depth-dependent spatial frequency of a reconstructed volume slice, λ is the wavelength of incident light, and M is the imaging objective magnification to describe the drop-off. Equation 2 applies only when $|z| \geq {p_l}^2/(2M^2\lambda)$, as the sampling requirement within the vicinity of the native object plane may not be met [17], but an aliasing-aware deconvolution algorithm can address some of these sampling artifacts [43]. This enables us to use high-speed cameras with relatively high pixel pitch and low pixel counts, which previously yielded intractably low total number of lenslets at the minimum practical p_p, to provide adequate 3D reconstruction for particle tracking.

LFM illumination sources must have spatial and angular uniformity as non-uniformities lead to intensity fall-off in the light-field images [15]. For fluorescent illumination, such as used here, only spatial uniformity is required, since the angular distribution of excited fluorescent point-sources (i.e., particles) is independent of the excitation light source.

2.2 2D synthetic light-field image generation

2D synthetic light-field images were generated to verify the implementation and to better understand any error sources such as, for example, lateral and depth-dependant aliasing, motion field characteristics, or signal to noise ratio (SNR), in the volume reconstruction, centroid localization, and particle tracking methods. Synthetic 2D light-field images were generated by applying ray transformation operations, diffraction effects, and noise sources through the optical path transform functions of the light-field system. Fig. 1a shows a schematic representation of the light path in the light-field microscope. Light rays travel from the object space, through the microscope objective and subsequent internal microscope optics to the side-port. The microlens array is placed at the focal plane out of a side-port of the microscope. Once light passes through and travels the focal length of the microlens array, f_l, the relay lens directs rays to a camera sensor, ultimately collecting the light-field pattern. The values used in the synthetic image generation were the nominal values as specified in the experiments, and are outlined in Table 1. To generate synthetic images, rays are traced through a simplified version, i.e., lumped transfer function, of the experimental setup and are discussed in further detail below.

To begin the synthetic image generation, for a given point-like light-emitting particle, i, in the field of view, several tens of thousands of light rays originating from a single point in object space at a position (x_i, y_i, z_i) and at a normalized scalar intensity are initialized. Each ray originating from the position, (x_i, y_i), and angle, (θ_i, ϕ_i), must translate a distance, $t_i = s_o + z_i$, to the front aperture of the imaging objective, where s_o is the distance from the native object plane to the front aperture of the microscope objective. The angular sweep of rays is defined with respect to the size of the front aperture, p_m, of the receiving lens to ensure rays only within the physical angular limits of the objective aperture, i.e., within the numerical aperture (NA), are accepted. The angular sweep of rays within the bounds of the optical system, $\theta_{max,min}$ and $\phi_{max,min}$, are defined as

$$\theta_{max,min} = \tan^{-1}\left(\frac{-x \pm p_m/2}{z + s_o}\right) \tag{3}$$

and

$$\phi_{max,min} = \tan^{-1}\left(\frac{-y \pm p_m/2}{z + s_o}\right) \tag{4}$$

Rays emitted from a given coordinate in object space must fall within the angular bounds of the receiving lens, which contribute to the achievable axial depth in a reconstructed volume of a given light-field system. Given this geometrical constraint, rays are traced from object space to the front aperture of the imaging lens. This linear propagation of light through free space is given by:

$$\begin{bmatrix} x_i' \\ y_i' \\ \theta_i' \\ \phi_i' \end{bmatrix} = \begin{bmatrix} 1 & 0 & t_i & 0 \\ 0 & 1 & 0 & t_i \\ 0 & 0 & 1 & 0 \\ 0 & 0 & 0 & 1 \end{bmatrix} \begin{bmatrix} x_i \\ y_i \\ \theta_i \\ \phi_i \end{bmatrix} \tag{5}$$

with transformed coordinates $(x_i', y_i', \theta_i', \phi_i')$. Next, the rays must propagate from the imaging objective to the microlens array. In the experimental light path, rays propagate through additional microscope optics including the multi-element microscope objective, filter cube, and tube lens. However, with the concept of principal planes, this combination of lenses can be reduced to a single thin lens approximation [31], which is referred to as the main lens. With this simplification, the effective focal length, f_m, can be calculated based on the experimental parameters. Thus, light traveling through the main lens with a calculated effective focal length can be transformed via

$$\begin{bmatrix} x_i'' \\ y_i'' \\ \theta_i'' \\ \phi_i'' \end{bmatrix} = \begin{bmatrix} 1 & 0 & 0 & 0 \\ 0 & 1 & 0 & 0 \\ -\frac{1}{f_m} & 0 & 1 & 0 \\ 0 & -\frac{1}{f_m} & 0 & 1 \end{bmatrix} \begin{bmatrix} x_i' \\ y_i' \\ \theta_i' \\ \phi_i' \end{bmatrix} \tag{6}$$

The ray tracing operations defined above describe the light transformations from object space, through the main lens and to the surface of the microlens array, placed at the conjugate native object plane. Next, the light must propagate through the microlens array to the camera sensor. The ray transfer operation defined in equation 6 assumes the lens is centered along the optical axis. However, in the case of a microlens array, most lenslets are shifted from the optical axis. A derivation from Georgiev and Intwala [44] provides a ray tracing operation to account for light propagation through a lenslet at an offset, (s_x, s_y), from the optical axis as

$$\begin{bmatrix} x_i''' \\ y_i''' \\ \theta_i''' \\ \phi_i''' \end{bmatrix} = \begin{bmatrix} 1 & 0 & 0 & 0 \\ 0 & 1 & 0 & 0 \\ -\frac{1}{fl} & 0 & 1 & 0 \\ 0 & -\frac{1}{fl} & 0 & 1 \end{bmatrix} \begin{bmatrix} x_i'' \\ y_i'' \\ \theta_i'' \\ \phi_i'' \end{bmatrix} + \begin{bmatrix} 0 \\ 0 \\ \frac{s_x}{fl} \\ \frac{s_y}{fl} \end{bmatrix} \tag{7}$$

Once propagated through the microlens array, rays are mapped to the simulated camera sensor, where identified camera pixels record an intensity signal to obtain the synthetic light-field image. The focal length of the microlens array is typically 1 mm to 10 mm [17]. Thus, a relay lens is typically added to project the image onto the sensor; however, any added magnification due to this optic may be accounted for by calibrating the pixel pitch of the microlens array with the camera sensor.

To create synthetic light-field images sufficiently comparable to the experimental data to access the algorithm performance, the effects of diffraction and the size of fluorescent particle used must be considered. We can approximate the diameter of an in-focus particle and its diffraction spot size in an image by applying a Gaussian profile based on particle size, emission wavelength, as well as the imaging lens magnification and numerical aperture [45]. From this approximation, it is determined that the finite particle diameter for the optical configuration used here has a negligible effect since the fluorescent particle image translates to less than one pixel on the camera sensor, and diffraction spot size of a particle is larger than the geometric size of the particle on the camera sensor itself. Thus, accounting for diffraction effects at the surface of the microlens array and camera sensor is necessary, and modeled by applying Gaussian white noise to the ray propagation at the surfaces of the microlens array and camera sensor in the synthetic images during ray tracing. Additionally, to model the primary noise present within an experimental light-field image, Gaussian white noise was also added directly to the synthetic images intensity values after ray tracing. A range of noise levels were added to determine algorithm sensitivity to sensor noise floor (see Section 4.1). Further information on the derivation of a 2D light-field simulation, from which this work was adapted, can be found in Lynch *et al*. [31].

2.3 Procedure workflow

Figure 2 shows the overall process to reconstruct displacement and strain information from 2D light field image sequences using particle tracking. This is a three step process consisting of the experimental setup, volume reconstruction, and post-processing to track particles, which provides displacement and strain fields throughout the volume. While the first two steps focus on the tomographic reconstruction of the imaged particles, discussed above, the last step requires the application of a 3D single particle tracking technique to reconstruct the 3D, volumetric displacement and strain fields. Here, we utilize an open source particle tracking framework [41] within which specific adaptions for LFM volumes to provide both high resolution displacement and strain information have been developed. To apply this algorithm, two key assumptions are made: the specimen is prepared with a relatively low seeding density of fluorescent particles (tens to hundreds of particles per imaging volume) and it undergoes an arbitrary, but spatially differentiable (i.e., kinematically admissible) mode of deformation during the experiment. Our synthetic and experimental validation, including specimen preparation, are detailed in Section 3.

3 Methods

3.1 Experimental methods

3.1.1 LFM optical system

A schematic of the complete system is shown in Fig. 1. The base microscope is an inverted epifluorescent unit (Nikon Ti-2, Melville, NY[1]) with a widefield high-intensity LED-based excitation source to provide spatially uniform fluorescent excitation. A chromatically corrected microscope objective (4×/0.20 NA; Nikon, Melville, NY) is used as the main imaging lens, with the numerical aperture matched to the microlens array (RPC Photonics, Rochester, NY) that has a nominal 100 μm lens pitch and 0.20 NA (f-number, f/10). Optical parameters, identical to those employed for the system simulation, are further outlined in Table 1. A high-speed camera (Phantom v2511, Vision Research, Wayne, NJ) with color sensor (28 μm square pixels, 12 bit depth) recording with a global shutter at a full-frame resolution of 1280 px by 800 px at up to 25 800 fps was used at full resolution and exported to 8-bit greyscale .tif image files. A tetramethylrhodamine isothiocyanate (TRITC) filter cube was used for imaging fluorescent polystyrene microspheres (or "particles", our fiducial markers; Invitrogen, Carlsbad, CA) with excitation and emission wavelengths at approximately 580 nm / 605 nm. These particles were chosen to optimize signal to noise by pairing the dye emission wavelength to a maximum of the quantum efficiency of the color camera sensor, and selecting a relatively large particle surface area.

3.1.2 Single layer particle preparation

A procedure for depositing a single layer of sparsely seeded particles on a glass coverslip was adapted from previously published protocols [40,46]. In short, 25 mm nominal diameter glass coverslip surfaces were fully coated with 0.1 mg/mL of Poly-D-lysine and left for approximately 1 hour. Coverslip surfaces were then dried using compressed air. An as-received solution of nominally 15 μm particles was sonicated for approximately 15 minutes, diluted to nominally 2 % mass fraction in water, and vortexed for about 30 seconds. This solution was pipetted onto the poly-D-lysine coated coverslip surface, left for approximately 30 minutes, and dried with compressed air again. This procedure yields a coverslip with a single layer of sparsely seeded particles that are well-adhered to the glass. These specimens were used for rigid body experimental validations and single particle visualizations.

3.1.3 Gel sample preparation

Polyacrylamide (PA) hydrogels were prepared according to established techniques [34] with a concentration of acrylamide to bis-acrylamide solution (Bio-Rad Laboratories, Hercules, CA) of nominally 10 % and 0.06 % volume fraction respectively and chemical cross-linking catalysts of 1.25 % Ammonium Persulfate (APS) and 0.5 % N,N,N',N'-tetramethylethane-1,2-diamine (TEMED) (Thermofisher Scientific, USA) volume fraction. Pre-polymerized solutions were cast in custom cylindrical molds (see [42]) with a nominal diameter of 10 mm and a gel height of approximately 3.7 mm prior to swelling. Care is taken to avoid and minimize air bubbles, meniscus

[1] Certain commercial equipment, software and/or materials are identified in this paper in order to adequately specify the experimental procedure. In no case does such identification imply recommendation or endorsement by the National Institute of Standards and Technology, nor does it imply that the equipment and/or materials used are necessarily the best available for the purpose.

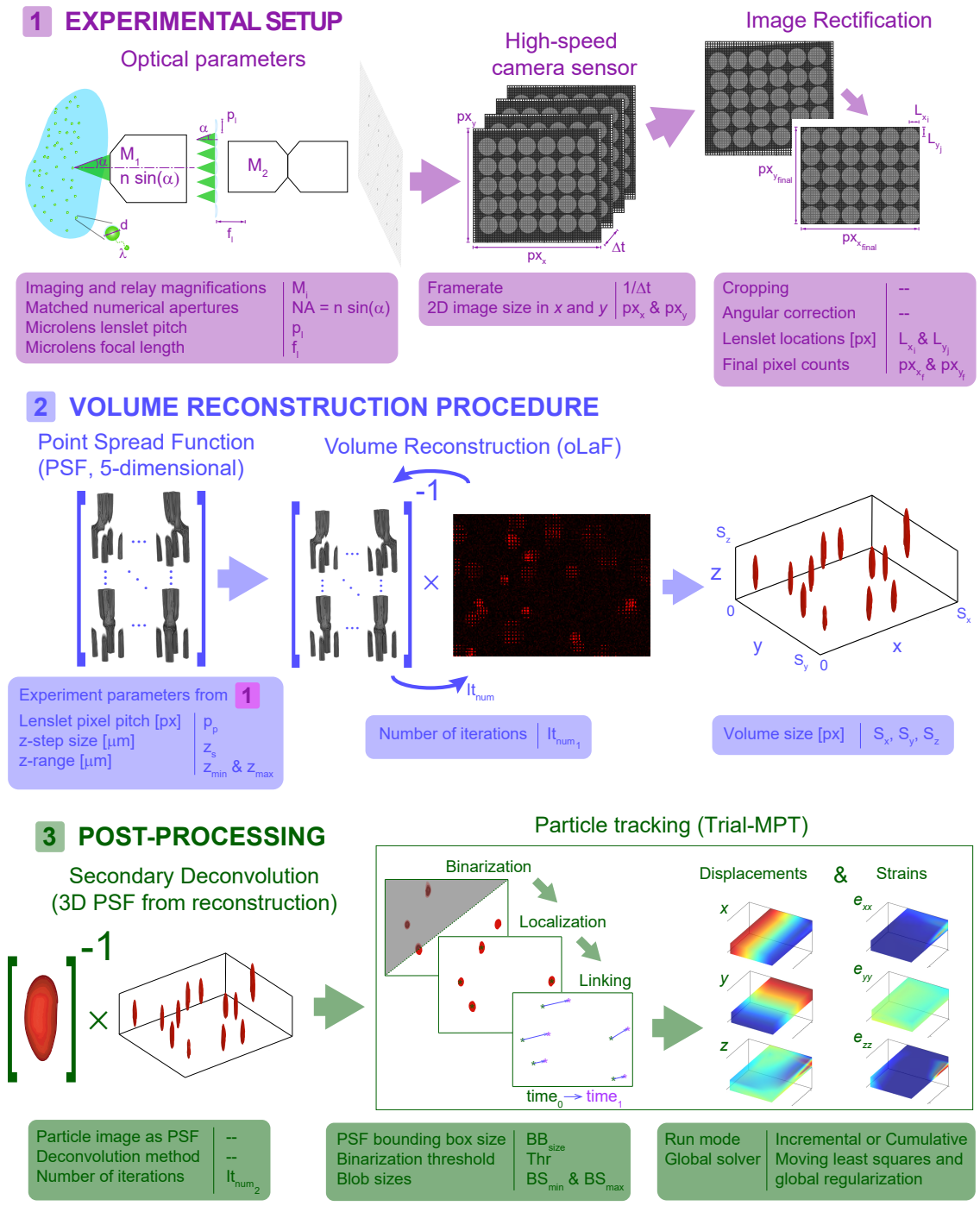

Fig. 2 Workflow diagram of the major steps and user-specified parameters to compute volumetric displacement and strain fields with a light field microscopy system. First, the optics and configure the optical train are defined and the image sequence is collected and rectified. Second, a synthetic point spread function (PSF) of the microlens array system is created and used to deconvolve the recorded 2D images, thus reconstructing the volumetric representation. Third, a single particle is segmented via a bounding box and used to perform secondary deconvolution, and the particles in each deconvolved volume are localized to sub-pixel accuracy and tracked across frames to obtain volumetric displacement and strain fields.

effects and other artifacts that could affect the homogeneity and geometric regularity of the specimen. The total gel height consisted of two layers of PA in two casting steps. The layer closest to the microscope objective (the bottom layer) was doped with nominally 15 μm fluorescent particles at a volume fraction of 0.01 % and the top layer was undoped. This double-layer preparation minimizes out of focus diffuse light that tends to cause diffraction artifacts during LFM reconstruction. The undoped and doped layers of polyacrylamide were cast within seconds of each other to allow the layers to cross-link, since the catalyzed crossing-link proceeds within minutes. The entire gel

volume was left to polymerize on a plasma treated and hydrophillicaly functionalized glass-bottomed 34 mm dish for approximately 30 minutes before experiments were conducted.

3.1.4 Shear Device

To impose controlled displacements on soft materials a stage-top *in-situ* simple shear impact device [47] (see 3) was designed and built. Similarly to a more conventional shear rheology instrument (e.g., separate motor-transducer type instruments used for large-amplitude oscillatory shear (LOAS) experiments [48]), the specimen is first gripped by bringing the movable platen into contact with the top of the specimen under displacement control

Table 1 Process parameters used for the signal to noise and displacement volume validations, single-layer validations, and the shear experiment. Except for differences as noted, synthetic and real condition were conducted with matched parameters. Codes: "S" synthetic experiments, "E" physical experiments.

Parameter	*SNR and Volume validations*	*Single-layer validations*	*Shear Experiment*
Experiment parameters			
Objective magnification, M_1 (Numerical aperture)	4X (0.2 NA)	4X (0.2 NA)	4X (0.2 NA)
Relay magnification, M_2 Numerical aperture	4X (0.13 NA)	4X (0.13 NA)	4X (0.13 NA)
Emission wavelength, λ (nm)	605	605	605
Particle size (μm)	15	15	15
Lenslet pitch, p_l (μm)	100	100	100
Microlens focal length, f_l (μm)	1000	1000	1000
2D image size in x and y ($\text{px}_x \times \text{px}_y$)	S: 1280×800 E: $\approx 600 \times \approx 650$	S: 1280×800 E: $\approx 600 \times \approx 650$	$\approx 600 \times \approx 620$
Framerate, frames/s, (1/s)	Quasistatic	Quasistatic	1000
Volume reconstruction parameters			
μm-per-pixel conversion (x and y)	1.64 $\frac{\mu m}{\text{px}}$	1.64 $\frac{\mu m}{\text{px}}$	1.64 $\frac{\mu m}{\text{px}}$
z-step size, z_s (μm)	5.0	5.0	5.0
z-range z_{min} to z_{max} (μm)	S: -80 to 720 E: -800 to 260	S: -80 to 720 E: -800 to 260	-730 to 370
Lenslet pixel pitch, p_p (px)	15	15	15
Number of iterations, It_{num_1}	3	3	3
Lanczos filter width	2	2	2
Volume size, $S_x \times S_y \times S_z$ (px)	S: $797 \times 1275 \times 101$ E: $635 \times 675 \times 181$	S: $797 \times 1275 \times 201$ E: $719 \times 767 \times 213$	$791\times 697 \times 221$
Post-processing parameters			
PSF bounding box size, BB_{size} (px)	$51 \times 51 \times \approx 90$	$51 \times 51 \times \approx 140$	$51 \times 51\times \approx 105$
Binarization threshold, Thr	0.25	0.3	0.08
Blob sizes, BS_{min} to BS_{max} (px^3)	1000 to 5000	500 to 18000	200 to 14000
Number of particles for PSF, N_{PSF}	1	1	2
Run mode (incremental or cumulative)	Inc	Inc	Inc
Deconvolution iterations, It_{num_2}	5	5	5
Outlier threshold	3	4	8
Global solver type	2	2	2
Regularization smoothness	0.05	0.05	0.03
Max number of neighbors	16	8	16

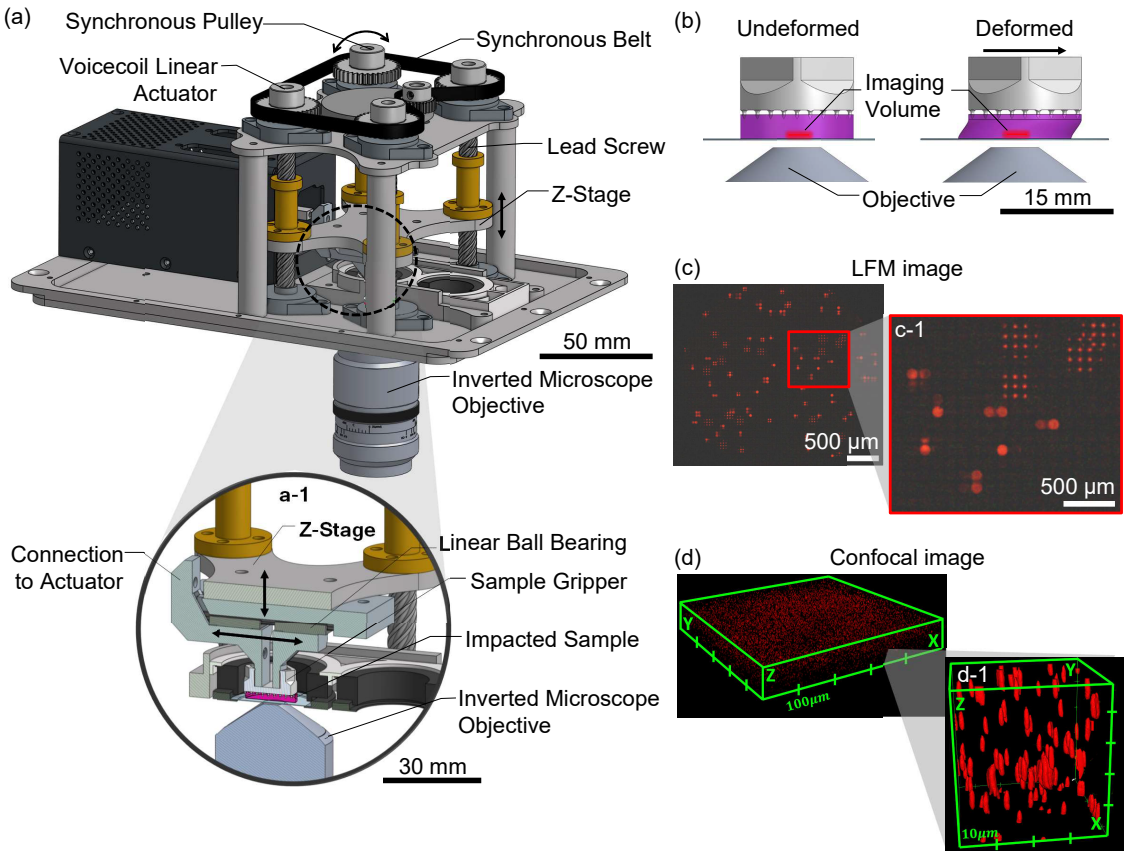

Fig. 3 The shear impact device used for demonstration experiments. (a) Rendered view of the complete device, including the voicecoil linear actuator to drive the shear motion via magnetic coupling, the synchronously driven z-stage control with anti-backlash nuts on a screw-type mechanism for vertical motion control and alignment, and inset *a-1*, a cutting plane detailing the specimen attachment to the bottom coverslip and top grip. (b) Schematic of the simple shear deformation applied during and impact event, with a typical imaging volume shown in red. (c) Example light-field view of a gel with fiducial marker particles seeded in the imaging volume, inset *c-1* shows a magnified view of one such particle. Brightness enhanced for viewing. (d) High-resolution multi-photon microscopy image volume of a similarly seeded gel volume, as an example of a typical quasi-static volume image with fiducial markers. Inset *d-1* shows an expanded view of several individual marker particles.

via four synchronized lead-screws (see 3a). However, unlike conventional shear rheology, which typically relies on friction modifications or chemical treatments of the platen to grip soft gels, a barbed gripper design is used to lightly puncture the surface of prefabricated soft materials at many points, while leaving a gap between the top of the test specimen and the flat face of the gripper above the barbs (see 3b). Contact force is only due to puncture force necessary for the barbs to embed into a given material, preventing interfacial slip during shearing while limiting pre-compression applied to the sample. This minimally invasive connection facilitates non-destructive material testing of compression-sensitive soft materials via a mechanical connection to the specimen surface.

The simple shear deformation was applied by transverse actuation of the top platen via a voicecoil linear actuator with custom tuning for given experimental configurations. The example impact demonstrated here applied a nominally 30 % engineering shear strain at nominally 2.0 s^{-1}, and LFM frames were acquired at a frame rate of 500 fps (Fig. 3c). Since the device is integrated into a microscopy stage insert, pre- and post-impact quasi-static imaging is straightforward, see for example the multiphoton-excitation based volume image in Fig. 3d. Additional impacts, not shown, were conducted at 20 s^{-1} and 40 s^{-1} to 30 % engineering shear with particle tracking at frame rates 1000 fps and 2500 fps respectively.

3.2 Volume reconstruction and particle tracking

Volume reconstruction and particle tracking are the two primary computational steps used to obtain volumetric displacement and strain fields from the raw 2D images. The complete process is implemented as a single script that incorporates a Flexible 3D Reconstruction Framework for Light Field Microscopy (oLaF) described by Stefanoiu *et al* [43] and the ScalE and Rotation Invariant Augmented Lagrangian Particle Tracking (SerialTrack) algorithm of Yang *et al*. [41] and iterates through a given sequence of light field images from a recording. The complete code

and datasets [49] used in this paper are provided free and open source (see Data Availability below). Although both oLaF and SerialTrack are described elsewhere (viz., [43,41]), a brief summary of both follows.

The core of the light-field deconvolution algorithm was described by Broxton *et al.* [17] and employs a wave optics-based model of the optical system for volume reconstruction, which improves axial and lateral resolution over geometric optics approximations (e.g., [15,22]). In addition, computed super-resolution is leveraged to combine aliased pinhole views for sub-lenslet sampling [17]. The reconstruction stage of HR-VPTM uses a lightly modified version of the open source reconstruction package "oLaF" [43], which implements a wave-optics reconstruction and automatic lenslet image calibration procedure. It begins by pre-processing the input images using a calibration with a uniformly illuminated field of view to identify lenslet centers and geometrical corrections. The system PSF is then synthesized using user-provided optical configuration parameters. The 2D time-series of images is then deconvolved with this PSF through an iterative depth-dependent and aliasing-aware deconvolution algorithm. Although some aliasing inevitability remains, particularly when operating at or near the native image focal plane, this approach typically reduces aliasing artifacts to below the noise floor when sufficiently far (ca. 80 μm to 100 μm) from the native image plane. Reconstructed volumes are saved as the input images for the particle tracking routine.

Particle tracking consists of, first, localizing the particle centroids with subpixel accuracy, and second, iteratively matching particles between image pairs. After particles are tracked the cumulative displacement field and deformation gradients are computed. For these steps, a co-developed version of the open source particle tracking algorithm SerialTrack [41] was employed. To begin, as with reconstruction, algorithm settings are specified based on the experimental conditions (see Table 1 for examples). For LFM-type reconstructions, a bespoke particle binarization routine is implemented – in this step, the volume images are pre-processed by selecting a bounding box (or bounding boxes) of one or more particles in the first volume of an experimental sequence and using the mean of the selected particle images as a point spread function to deconvolve the volumes. Binary blobs of particles in the deconvolved volumes are segmented from the background via active contours. A minimum and maximum binary region size per particle is chosen by the user based on a histogram of sizes, and the binary regions input to the localizer are down-selected using these limits, thereby avoiding tracking reconstruction artifacts, noise, particle clumps and other unreliable fiducials. The accepted binary regions are passed to a center-finding method [50] to localize the reconstructed particle positions with sub-pixel accuracy. For each particle position in a given volume image pair, a feature vector based on the local topology of neighboring particles is used to establish initial particle match guesses between volumes. The algorithm adaptively selects, on each iteration, histogram-of-position based feature vector with link verification [39], neighborhood topology, or histogram-of-displacements methods [51], or a simple first nearest-neighbor feature depending on the number of particles identified and successfully tracked. These techniques are generally robust to loss of particles, addition of particles, and large relative change in local positions within a given neighborhood [39,41]. The particle displacement field and matching guesses are iteratively refined using a global regularization to enforce kinematic admissiblity. The local deformation gradient for each particle is computed from least-squares fitting of the local neighborhood of displacements as a precursor step to the global regularization (see [41] for details). Alternatively, the user has the option to compute strains directly using a spatial gradient filter of the interpolated, gridded displacement field if an Eulerean reference frame is used. From the incremental pair-wise data, total cumulated full-field displacement vectors and strain tensors are then computed and stored using either an Eulerean – i.e., grid-interpolated incremental displacement and strain with finite deformation cumulation (see [52] and [41]) – or Lagrangian – i.e., total particle displacement via track linking with gridded displacement and strain interpolated at the frame of interest (see [41]) – framework. In either case, the final cumulative displacements and strain are displayed and saved.

4 LFM particle tracking measurement validation

This section describes the synthetic and experimental verification and validation of HR-VPTM. Optical parameters and tracking settings for each of the cases are reported in Table 1. Synthetic experiment parameters are chosen based on the experimental setup. Thus, unless otherwise specified, synthetic images are generated with independent Gaussian noise at an SNR of nominally 17.

To evaluate uncertainty two metrics were used. For the synthetic validation cases, where the applied displacement ground truth is known, a root mean square deviation (RMSD) was calculated between the reconstructed and imposed measurement points. Here, RMSD is defined as $RMSD = \sqrt{(\sum(x_i - x_0)^2)/n}$, where x_i is the measured signal, x_o is the imposed signal and n is the number of measurement points (typically particles) in a volume, which can vary as particles enter or leave the field of view. In the experiments, a nominal commanded displacement is imposed, but the ground truth is not known. Therefore standard error is used as a metric to to quantify measurement uncertainty for the experiments. The standard error is defined as $\sigma_{err} = \sigma/\sqrt{n}$, where σ is the standard deviation of measurement signal over all finite measurement points in the volume, and n is the number of measurement

points in the volume, which, as before, can vary as particles enter or leave the field of view. Validation cases shown represent data from typical single experimental repeats. In preliminary work, results were shown to be repeatable, given that correct preparation procedures and settings were employed.

For volume reconstruction, the lateral field of view (i.e., total magnification) was selected via choice of imaging optics based on the coupling between lateral resolution and field of view, and the total required depth-of-field based on volume reconstruction quality (see Eq. 2) and expected experimental requirements. The depth-dependency of lateral resolution [17,43], creates a balance between aliasing error near the native object plane and spatial resolution decay far away from the native image plane. Thus, synthetic and experimental volumes were biased either above or below the native object plane, and a pixel pitch in the z-direction of 5 μm/pixel was used throughout.

To obtain in-plane pixel pitch, i.e., the relationship between the native pixel dimensions of the camera and physical dimensions, an initial calibration step was required. This is obtained via a light-field image of a stage micrometer that was computationally generated for the synthetic cases and directly acquired for the experimental cases. Using the micrometer divisions in the synthetic and experimental calibration volumes, a micrometer-to-pixel conversion ratio of approximately 1.64 μm/pixel was measured for each. In synthetic cases, where the full camera resolution is used, the field of view is approximately 2100 μm by 1300 μm. For experimental cases where a cropped image is used due to vignetting in the microscope, the field of view is approximately 975 μm by 1100 μm. See Table 1 for details of each configuration.

4.1 Zero-displacement noise floor

To quantify the zero-displacement noise floor, first, the localization error of recovered positions with respect to ground truth positions was measured. A synthetic volume was initialized in object space, providing a ground truth for point-source locations. Using this set of coordinates, a series of light-field images were generated with additive white Gaussian noise at signal to noise ratios (SNR) ranging from 90 (best-case) to 5 (worse-case). Light-field images were then processed to obtain a measured centroid location (i.e., localization) for each particle. Fig. 4a shows the absolute position error for the localization and RMSD between the ground truth and and recovered centroid locations as a function of SNR. The maximum absolute error and RMSD in the x-, y-, and z-directions was 0.35 μm $\pm$ 5.2 μm, 0.34 μm $\pm$ 3.2 μm, and 3.5 μm $\pm$ 9.5 μm respectively.

Next, zero-displacement image pair reconstructions were used to quantify the displacement measurement accuracy at a range of noise levels. Using the same image generation process as the localization error image sequence, zero-motion image pairs were constructed at SNR values from 90 to 5 with independent white noise in each image. Displacements were measured between each image in the pair. In Fig. 4b the mean displacement error and RMSD of tracked particles as a function of SNR are plotted. The relatively flat absolute error and RMSD demonstrates that the technique is robust to noise up to noise levels substantially higher than those in the circa 1000 fps experiments, see the dashed line in Figs. 4b and 4c.

To quantify the effect of frame rate (and thus exposure time) on the zero-displacement noise floor, experimental light-field images of a seeded hydrogel were captured at camera frame rates from 100 fps to 25 000 fps. As the camera frame rate increases, and hence exposure time proportionally decreases, the system becomes light starved with sensor noise largely driven by frame-rate-based gain requirements. A series of three zero-displacement images were recorded at each frame rate and used to calculate inter-frame grey-level SNR (one standard deviation of pixel-wise 8-bit grey level variation over three shots) at each camera frame rate, shown on the right axis of Fig. 4c. Approximately 65 particles were in the field of view for synthetic images and 20 for the experimental images. On the left axis of Fig. 4c, the absolute and RMSD displacement errors show that that as frame rate increased the measurement noise floor stayed relatively constant until 4000 fps, where integration time becoming insufficient to collect particle fluorescence. This uncertainty level is consistent with the synthetic validation in Fig. 4b.

4.2 Rigid body displacement measurement validation

To quantitatively determine lateral and axial rigid body displacement uncertainty, two test configurations were used for both synthetic and experimental cases. For axial resolution, it was important to investigate the upper and lower focusing limits, specificity for which was achieved by employing a single layer of particles that are translated from extreme bottom to top of the imaging volume. Lateral resolution is nominally constant across the field of view, but may be subject to artifacts (e.g., lenslet aliasing) in volume reconstruction. Thus, fully 3D seeded volumes were used to account for coupling between z-position and these artifacts over a smaller range of displacement. Specifically, for lateral resolution, in-plane rigid body displacement was applied both synthetically to a 300 μm tall volume randomly seeded with particles and experimentally on a hydrogel sample. In-plane sequential rigid body displacements with increments of 5 μm were applied independently in the x- and y- directions. For axial

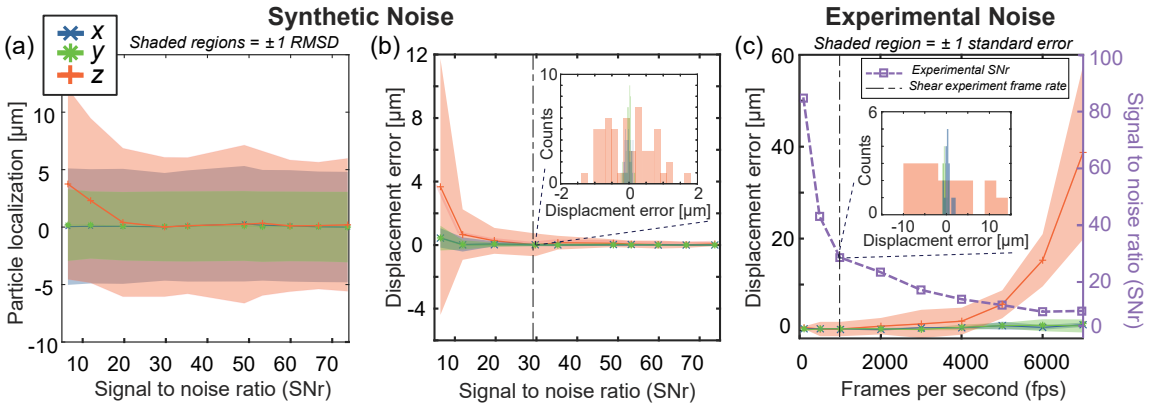

Fig. 4 (a) Localization position error of ground-truth particle locations with respect to measured particle positions for a range of signal to noise ratios (SNR). (b) Reconstructed displacement error for zero-displacement image pairs with the shaded region showing the RMSD error (shaded area, $n \approx 65$) plotted against increasing SNR. The vertical dashed line indicates the noise level used in validations and measured in the experimental demonstration. (c) The experimental zero-motion pair displacement error and standard error (shaded area, $n \approx 20$) as a function of camera frame rate (left axis). The corresponding image shot noise is also plotted against camera frame rate for comparison (right axis, one standard deviation of grey-levels in three snapshots, note that camera settings were adjusted appropriately for each frame rate). *Insets* Histograms of displacement error at SNR ≈ 30 (the approximate experimentally observed noise level in the demonstration experiment).

resolution, a single layer of point-sources for the synthetic images, and a single layer of particles adhered to a glass microscope slide for the experiments, was positioned at 160 μm above the native focal plane and sequentially displaced in increments of 20 μm upward to 500 μm. Mean error and RMSD were measured for one sequence (preliminary data showed good repeatably between successful runs) with approximately 40 particles for volumes and 15 particles for single layers for experiments and approximately 75 particles and 20 particles respectively for synthetic images.

In synthetic test cases, measured displacement uncertainty agreed with sub-pixel accuracy to the applied in-plane displacements, with RMSD in the x-, y-directions, of $\pm 0.60\,\mu$m, $\pm 0.59\,\mu$m (Fig. 5a). Agreement in nominally zero-displacement directions was comparable to the static noise floor (see Fig. 4), with maximum RMSD of approximately 0.2 μm in x- or y-directions and $\pm 3.2\,\mu$m in the z-direction, across the range of displacements tested. For the single-layer z-displacement cases, RMSD suffered considerably – an expected result since the number and distribution of particles was less suitable for the tracking algorithm and any aliasing was exaggerated – with maximum z-direction RMSD of $\pm 39.1\,\mu$m and nominally-zero displacement x- and y-direction RMSD of approximately $\pm 5.4\,\mu$m and $\pm 8.7\,\mu$m (Fig. 5b). Notably, at z-planes closer than approximately 240 μm to the native imaging plane reconstruction artifacts (see Eq. 2) increased the measurement uncertainty, and this effect remained noticeable in the first several z-steps where the maximum RMSD occurs. The inset error histogram at SNR = 30 shows a typical distribution of errors in the x-, y-, and z-directions. This demonstrates an approximately zero-mean normally distributed error consistent with random noise-driven uncertainty for x- and y-displacement. Axial errors were substantially broader and flatter, consistent with the resolution-limited nature of the z-direction uncertainty.

For the equivalent experiments, the mean measured displacements are plotted against nominal applied in-plane rigid body displacements. The correspondence is close to 1:1, and maximum standard error for the fully seeded volumes in the x-, y-directions of approximately $\pm 0.3\,\mu$m and approximately $\pm 1.6\,\mu$m in z-direction, across the range of displacement tested (Fig. 5c). For the single-layer z-displacement case, the maximum standard error in the z-direction displacement was approximately $\pm 3.0\,\mu$m, and x- and y-displacement standard errors were approximately $\pm 0.5\,\mu$m and approximately $\pm 1.0\,\mu$m. The inset error histogram confirms a similar nature of the error distribution.

4.3 Synthetic LFM volume deformation validations

As a final validation, synthetic volume deformations with homogeneous deformations were constructed to directly simulate typical experimental deformation fields including uniaxial tension and simple shear. Light-field images for incremental deformations, e.g., for each frame in a time-series, were generated with the optical parameters summarized in Table 1. Synthetic volumes approximately the same size as experimental volumes were created and the following synthetic deformations were applied:

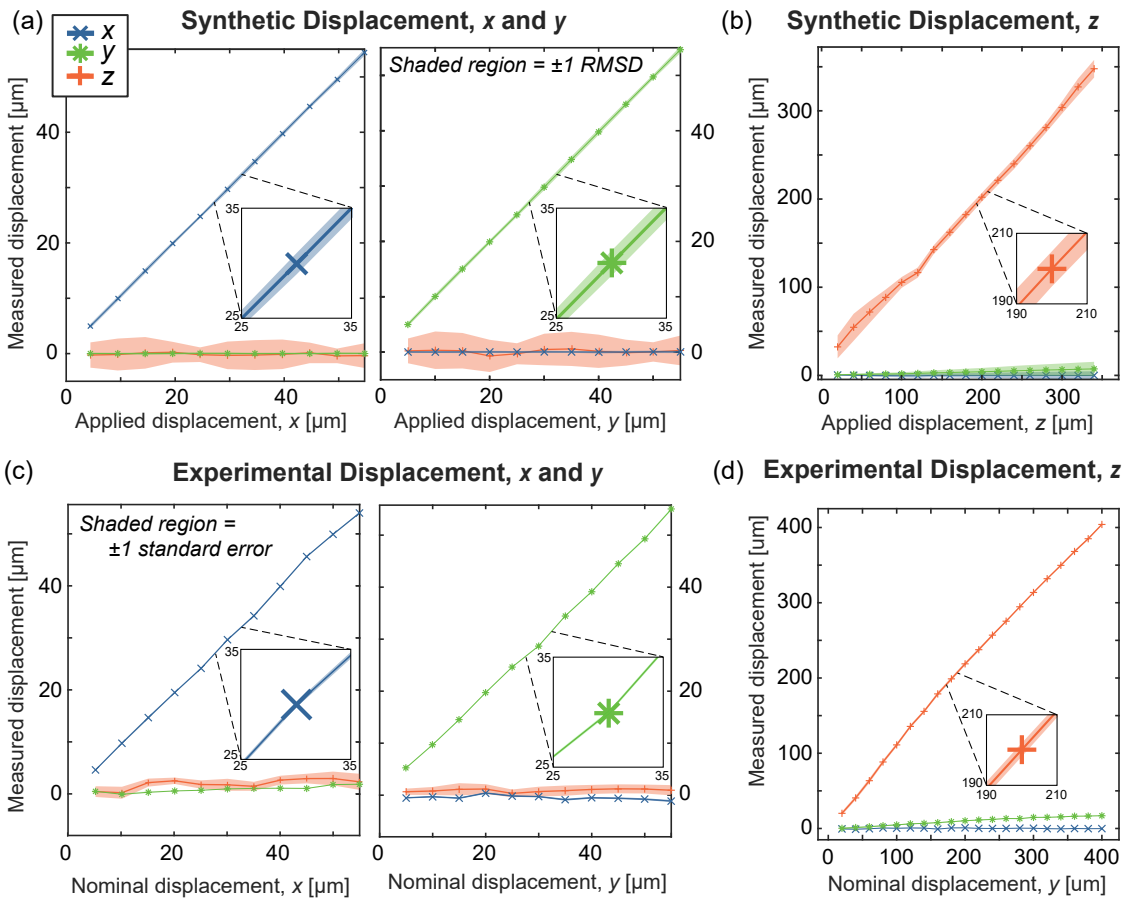

Fig. 5 Experimental and synthetic motion reconstruction uncertainty quantification in the x-, y-, and z- directions. (a) A synthetic light-field volume with incremental 5 μm displacements in the x- and y-directions, with resulting measured mean displacement and ± 1 RMSD errors (shaded area, $n \approx 50$) shown plotted against the imposed displacement. (b) A synthetic validation of z-direction motion reconstruction using a single layer of point-sources displaced in increments of 20 μm from 160 μm above the native object plane and progressing upward a total of 500 μm with resulting mean displacements and RMSD error (shaded,$n \approx 15$) plotted against the applied synthetic displacement. (c) The experimental equivalent to (a) - seeded hydrogel volumes were translated in x- and y-directions in nominal increments of 5 μm, with resulting measured mean displacement and standard error (shaded, $n \approx 50$) plotted against nominal displacement. (d) The resulting experimental mean displacement and standard error (shaded $n \approx 15$) for a single layer of fluorescent particles that were displaced in z in nominal increments of 20 μm starting at an initial position of approximately 160 μm and translating upward approximately 420 μm (note the drift in the y-direction is repeatable ($n = 3$) and likely a z-stage or alignment artifact).

1. **Uniaxial stress:** Uniaxial volume-preserving tension (i.e., $\epsilon_{xx} = \lambda - 1$, $\epsilon_{yy} = -1/\sqrt{\lambda - 1}$, $\epsilon_{zz} = -1/\sqrt{\lambda - 1}$ and all others zero, for stretch ratio $\lambda >= 1$) applied in the x-direction with axial engineering strain from 5 % strain to 25 % strain in increments of 5 % strain.
2. **Rigid body rotation:** Positive right-handed rotation centered about the z-axis applied from 5 ° to 45 ° in increments of 5 °.
3. **Simple shear:** Simple shear applied to the z-face in the x-direction (i.e., ϵ_{zx}) from 2.5 % engineering strain to 25 % strain in increments of 2.5 % strain.

For each synthetic deformation step, the 3D volume reconstruction and post-processing were conducted, and respective displacements and full-field strains were measured. Mean error and RMSD were computed against the known ground truth. For these volumes n ≈ 50 particles for displacement, which is interpolated onto a grid with approximately 50 000 nodes. The results are summarized in Fig. 6. Displacement uncertainties match well with those described for the zero- and homogeneous-displacement cases described earlier. Strain uncertainty (shaded area is ± 1 RMSD) in components other than e_{zz} and e_{zy} are typically less than 1 % strain with mean errors substantially smaller (one set of synthetic images, mean across tracking results from initially 50 to 60 particles in the field of view). The e_{zz} and e_{zy} components directly rely upon spatial differentiation in the direction of the noisy z-displacement and thus error and uncertainty are notably elevated. For the rigid rotation case, although no strain was applied in the z-direction, reconstruction artifacts that drive displacement and strain errors are coupled to both z-planes and spatial location of individual particles with respect to individual lenslets and the field of view. Strain is more sensitive to this noise since it relies upon displacement gradients, which inherently amplify the noise. For

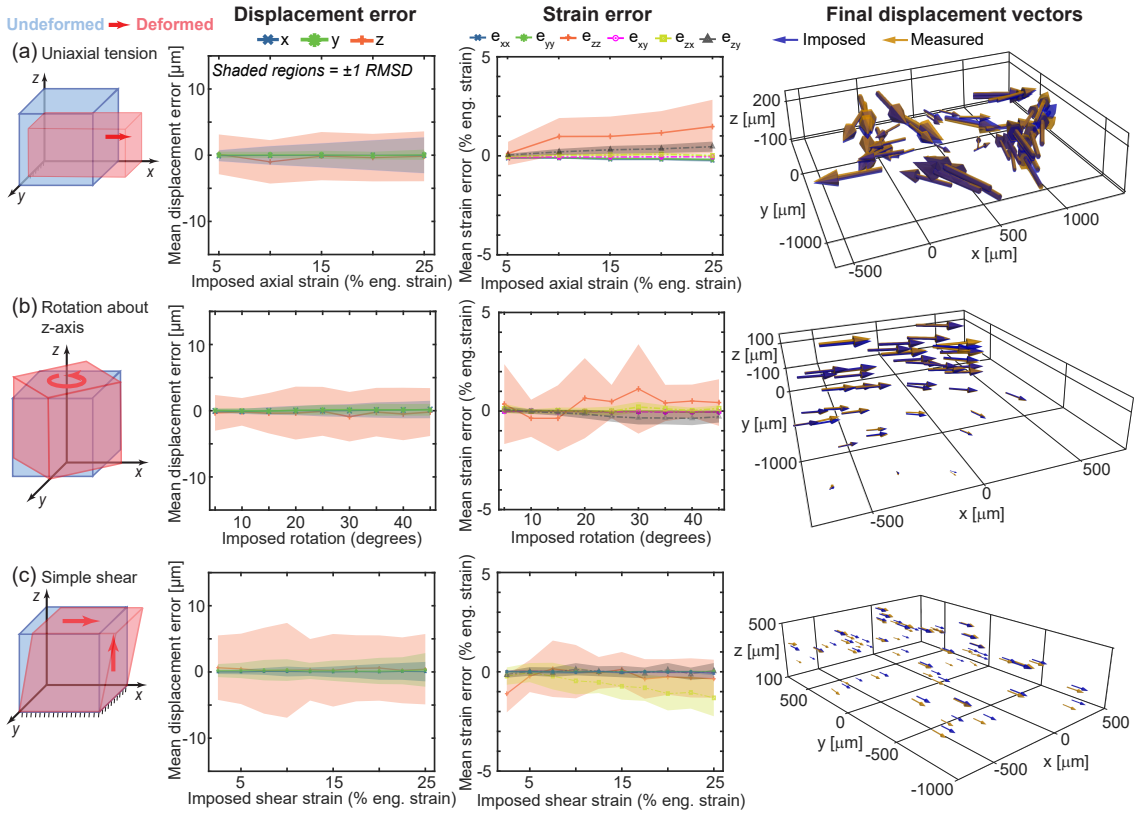

Fig. 6 Synthetic homogeneous deformation cases. Light-field images at the reference configuration and each increment were generated, reconstructed, tracked, and errors were computed on the cumulated quantities. Displacement and strain errors were computed per measurement point from the ground truth deformation function, and mean ± 1 RMSD were plotted (center column). Imposed particle displacement and measured displacement vectors for each particle are shown for the final maximum displacement configuration, in an arbitrarily offset coordinate system referenced to the reconstruction domain (right column). (a) Uniaxial volume conserving tension with cumulative engineering strain in the x-direction from 5 % strain to 25 % strain in increments of 5 % strain. (b) Rigid body rotation about the z-axis with rotation angles from 5 ° to 45 ° in increments of 5 °. (c) Simple shear from 2.5 % strain to 25 % engineering strain in increments of 2.5 % strain. Trend lines show mean error ($n \approx 50$) and shaded regions are ± 1 RMSD.

the simple shear case, measured strain in the applied shear component was slightly under-predicted. This reflects a common artifact in both particle tracking and image correlation related to the inherent low-pass filtering nature of these algorithms. From the vector plot overlay of imposed and measured particle displacements (right-side column), the offset errors apparent in Fig. 4a for particle localization are evident. However, the displacement vectors are substantially similar, which is consistent with the static image pair analysis in Fig. 4.

5 3D displacement and strain mapping of high strain-rate shear impact

Demonstration LFM experiments were conducted using a nominally simple shear impact at several rates. PA hydrogels seeded with fluorescent particles (see Sec. 3) were deformed using the custom *in-situ* simple shear impact device described in Sec. 3.1.4. See Fig. 3. In the example presented in the Fig. 7, the device was programmed to deform hydrogel samples to $\epsilon_{zx} = 30\,\%$ engineering strain at a nominal engineering strain rate of $2.0\,\mathrm{s}^{-1}$. To capture the cumulative applied displacements of the impact, it was important to optimize the temporal resolution of the imaging system by balancing frame-rate with fluorescent signal on the camera sensor. Given the optical and system parameters, data was recorded at nominally 500 fps. Once the shear device was brought into contact and aligned, the camera was initiated and internally calibrated. Prior to starting the impact, the camera was manually triggered, recording the reference configuration of the volume. Once the impact was started, the camera continued recording throughout the maximum observed shear displacement and until viscoelastic and inertial effects in the PA gel dissipated and the material reached its final deformed state. The 2D light field frames were then collected from the camera buffer for post-processing, i.e., deconvolution, particle tracking, and deformation reconstruction.

To summarize the result from a single example experiment, Fig. 7a includes representative light-field images of particles at the reference and maximum shear configurations with a reconstructed volume overlay showing particles in the reference (i.e., at time $t_{ref} = 0\,\mathrm{s}$, shown in blue) and maximum shear configuration (at approximately

time $t_{E_{max}} = 0.08$ ms, shown in red). The time history of Lagrange strain (**E**) as computed from the motor and as volumetrically measured via HR-VPTM (mean ± standard error, n = number of tracked particles, over the measurement volume) is shown in Fig. 7b. The observed maximum shear displacement slightly lagged and overshot the recorded motor motion displacement peak at approximately $t_{E_{max}} = 0.16$ ms. This is likely due to inertial and viscous effects in the PA gel, since the measurement volume is in the lower region of the hydrogel and displacement is applied at the top. The increasing-decreasing trend in E_{xx} is a typical hallmark of minor system misalignment. An increasing trend in the *zz*-component of Lagrange strain was an expected outcome of finite deformation simple shear (9 % strain in *zz* for a 30 % strain in *zx* is nominal), and closely matches between the experimental observation and the theoretical prediction. All these effects contribute to the total state of strain and effective strain rate in the material, but would be difficult or impossible to measure *in-situ* without volumetric measurement enabled by HR-VPTM. Slices taken through the cumulative volumetric displacement at the maximum deformation are shown in Fig. 7c, where the reconstructions show a *x*-displacement gradient in *z* for the *yz*-slice with comparatively little displacement in the *y*-direction. The resultant cumulative components of the Lagrange strain tensor are similarly shown in Fig. 7d.

6 Limitations for high-speed LFM system design

When designing a LFM system, selected sensors and optics dictate the spatial and axial resolution of reconstructed volumes. The choice in imaging objective and microlens array define the depth-dependent rate of lateral resolution fall-off. However, with the added complexity of high-speed imaging, the emission wavelength and size of the chosen fluorescent particles must be tuned to collect adequate signal on the camera sensor, and sensor pixel counts are typically small. Larger size fluorescent particles emit more light and thus provide stronger intensity signal for the camera sensor. Choosing large fluorescent markers dictates the seeding density of a given sample volume, since particle overlapping causes occlusion and non-uniqueness of the fluorescent signal for limited-angle tomography. Thus, seeding density must balance spatial resolution and particle overlapping in the field of view for adequate volume reconstruction and subsequent particle tracking. Particle seeding density and total particle count requirements for motion tracking (see, e.g., [39]) then affects the magnification and numerical aperture of the imaging lens, which in turn dictates the microlens array parameters. The experimental design choices here, see examples in Table 1, were chosen to meet these constraints for sample shear impact measurement goals. For this study, only commercially available optics and fluorescent markers were tested. However, future work may include custom-designed fluorescent markers with brighter emission signal at smaller particle sizes. With smaller particle sizes, LFM optics can be selected to increase axial resolution and brighter particles increase SNR (see Fig. 4).

In reconstructed 3D volumes particles tend to be elongated in the axial dimension. This is a result of the reduced axial resolution [32] and is related to the lateral and axial resolution trade-off of LFM. This limitation in the *z*-axis reconstruction is readily apparent in the roughly 1 order of magnitude higher noise in the *z*-direction uncertainty and error. Thus, when designing an experiment for HR-VPTM, care must be taken to account for the elevated noise floor in the *z*-direction, particularly if the principal quantity of interest for measurement is in the *z*-direction. While we have demonstrated a relatively generic system for the length- and time-scales considered, illumination, particles, optics and sensor are interrelated and may be optimized for a given figure of merit in the measurement.

7 Summary and Conclusions

In this study, we developed a light field microscope with accompanying post-processing routines to reconstruct 3D volumetric displacement and strain fields in soft materials undergoing high-rate deformations. This tool is termed High Rate Volumetric Particle Tracking Microscopy (HR-VPTM). Synthetic light-field images generated with experimental design parameters were used to bound uncertainty and validate the displacement measurement capabilities of our post-processing techniques. Synthetic and experimental validation and verification included rigid body axial displacement, rigid body rotation, uniaxial stress, and simple shear motion fields. As a practical example, a simple-shear impact device was built to deform soft PA gels at engineering shear strain rates up to $100\,s^{-1}$, and the LFM particle tracking retrieved the at-rate 3D volumetric displacement and strain fields from a trial experiment at $2\,s^{-1}$. Scripts for reconstruction, post-processing, and particle tracking are released as open-source tools (see Data Availability section). This novel microscopy-based capability fills a critical need for an accessible experimental means to measure high-rate volumetric deformations in soft materials.

Acknowledgements The authors thank Dr. Mohak Patel for early conversations, Dr. Jin Yang for fruitful discussions regarding particle tracking, Dr. Lauren Hazlett and Harry C. Cramer III for assistance with optical microscopy, and Dr. Young-Gyu Yoon for insights on LFM set

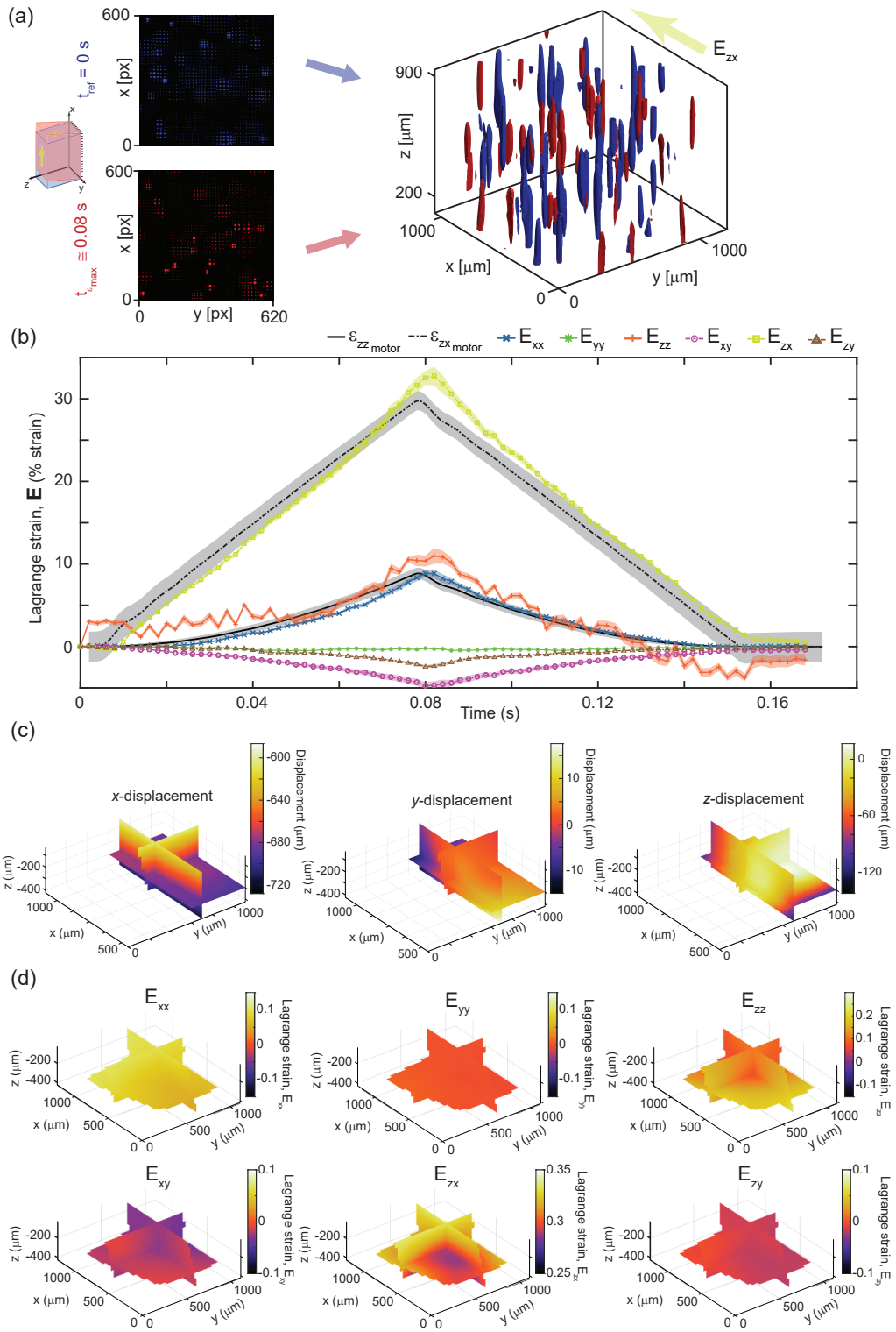

Fig. 7 (a) Raw LF images at reference and deformed configurations with reconstructed volumes overlayed (blue = reference at $t_{ref} = 0$ s; red = deformed at $t_{E_{max}} \approx 0.08$ s) (b) Mean strain history for each component of the Lagrange strain tensor from an example experiment conducted at nominally 2 strain/s, shown as mean ± standard error (with n = number of successfully tracked particles per frame). The black lines shows the recorded motor trajectory during the same experiment with shaded area showing uncertainty propagated from motor and gel details. (c) Contours of cumulative displacement components at the maximum deformation configuration. (d) Contours of the cumulative Lagrange strain components at the maximum deformation configuration. For (c) and (d) note the differences in color scale between plots. See online version for color.

up. Funding was partial provided via Dr. Timothy Bentley at the Office of Naval Research through grants N00014-17-1-2058 and N00014-21-1-2044 (PANTHER). The research was performed while A.K.L. held a NRC Research Associateship at the National Institute of Standards and Technology.

Data availability

Datasets and evaluation scripts used in the preparation of this paper - simulation, validation and shear - are available on the MINDS@UW server (`https://minds.wisconsin.edu/handle/1793/83031`). The HR-VPTM code used to analyze the data and to produce results shown in the figures above is available at `https://github.com/francklab/HR-VPTM`, where we will provide support for re-use as possible.

Author contributions

C.F., A.L., S.B., L.S., and A.C. conceived the study. A.L. and S.B. designed and implemented the LFM system and validations. L.S. designed the shear impact device. J.Z., L.S. and S.B. conducted experiments. S.B. adapted and developed synthetic image generation and test cases, and A.L. adapted and developed particle localization, tracking and post-processing scripts. A.L. and S.B. analyzed results and prepared figures, with contributions from L.S. and J.Z. for shear experiments. S.B. and A.L. wrote the manuscript with contributions from L.S. and A.C.. C.F. and A.L. oversaw analysis and experiments. All authors reviewed and approved the manuscript.

Conflict of interest

The authors declare that they have no conflict of interest. Certain commercial equipment, software and/or materials are identified in this paper in order to adequately specify the experimental procedure. In no case does such identification imply recommendation or endorsement by the National Institute of Standards and Technology, nor does it imply that the equipment and/or materials used are necessarily the best available for the purpose.

References

1. B.K. Bay, T.S. Smith, D.P. Fyhrie, M. Saad, Experimental Mechanics **39**(3), 217 (1999). DOI 10.1007/BF02323555. URL `http://link.springer.com/10.1007/BF02323555`
2. C.P. Neu, M.L. Hull, J.H. Walton, M.H. Buonocore, Magnetic Resonance in Medicine **53**(2), 321 (2005). DOI 10.1002/mrm.20343
3. J. Fu, F. Pierron, P.D. Ruiz, Journal of Biomedical Optics **18**(12), 121512 (2013). DOI 10.1117/1.JBO.18.12.121512. Publisher: International Society for Optics and Photonics
4. C. Franck, S. Hong, S.A. Maskarinec, D.A. Tirrell, G. Ravichandran, Experimental Mechanics **47**(3), 427 (2007). DOI 10.1007/s11340-007-9037-9
5. E.E. Hoover, J.A. Squier, Nature Photonics **7**(2), 93 (2013). DOI 10.1038/nphoton.2012.361
6. K. Chatterjee, K. Chatterjee, K. Chatterjee, F.W. Pratiwi, F.W. Pratiwi, F.W. Pratiwi, F.C.M. Wu, P. Chen, B.C. Chen, Applied Spectroscopy **72**(8), 1137 (2018)
7. G.M. Brown, Optical Engineering **39**(1), 10 (2000). DOI 10.1117/1.602438
8. J. Mertz, Optica **6**(10), 1261 (2019). DOI 10.1364/OPTICA.6.001261. Publisher: Optical Society of America
9. C.R. Copeland, C.D. McGray, B.R. Ilic, J. Geist, S.M. Stavis, Nature Communications **12**(1), 3925 (2021). DOI 10.1038/s41467-021-23419-y
10. J. Ren, K.Y. Han, ACS photonics **8**(3), 933 (2021). DOI 10.1021/acsphotonics.1c00012
11. S. Abrahamsson, M. McQuilken, S.B. Mehta, A. Verma, J. Larsch, R. Ilic, R. Heintzmann, C.I. Bargmann, A.S. Gladfelter, R. Oldenbourg, Optics Express **23**(6), 7734 (2015). DOI 10.1364/OE.23.007734
12. S. Abrahamsson, R. Ilic, J. Wisniewski, B. Mehl, L. Yu, L. Chen, M. Davanco, L. Oudjedi, J.B. Fiche, B. Hajj, X. Jin, J. Pulupa, C. Cho, M. Mir, M.E. Beheiry, X. Darzacq, M. Nollmann, M. Dahan, C. Wu, T. Lionnet, J.A. Liddle, C.I. Bargmann, Biomedical Optics Express **7**(3), 855 (2016). DOI 10.1364/BOE.7.000855
13. W. Shi, P. Dong, M.A. Kuss, L. Gu, F. Kievit, H.J. Kim, B. Duan, Advanced Healthcare Materials p. 2100180 (2021). DOI https://doi.org/10.1002/adhm.202100180
14. J.B. Estrada, H.C. Cramer, M.T. Scimone, S. Buyukozturk, C. Franck, Brain Multiphysics **2**, 100034 (2021). DOI 10.1016/j.brain.2021.100034
15. M. Levoy, R. Ng, A. Adams, M. Footer, M. Horowitz, in *ACM SIGGRAPH 2006 Papers on - SIGGRAPH '06* (ACM Press, Boston, Massachusetts, 2006), p. 924. DOI 10.1145/1179352.1141976. URL `http://portal.acm.org/citation.cfm?doid=1179352.1141976`
16. H. Li, C. Guo, D. Kim-Holzapfel, W. Li, Y. Altshuller, B. Schroeder, W. Liu, Y. Meng, J.B. French, K.I. Takamaru, M.A. Frohman, S. Jia, Biomedical Optics Express **10**(1), 29 (2019). DOI 10.1364/BOE.10.000029
17. M. Broxton, L. Grosenick, S. Yang, N. Cohen, A. Andalman, K. Deisseroth, M. Levoy, Optics Express **21**(21), 25418 (2013). DOI 10.1364/OE.21.025418
18. M. Martínez-Corral, B. Javidi, Advances in Optics and Photonics **10**(3), 512 (2018). DOI 10.1364/AOP.10.000512
19. J.H. Park, K. Hong, B. Lee, Applied Optics **48**(34), H77 (2009). DOI 10.1364/AO.48.000H77

20. G. Wu, B. Masia, A. Jarabo, Y. Zhang, L. Wang, Q. Dai, T. Chai, Y. Liu, IEEE Journal of Selected Topics in Signal Processing **11**(7), 926 (2017). DOI 10.1109/JSTSP.2017.2747126
21. P. Anglin, S.J. Reeves, B.S. Thurow, IEEE Journal of Selected Topics in Signal Processing **11**(7), 1020 (2017). DOI 10.1109/JSTSP.2017.2747481
22. R. Prevedel, Y.G. Yoon, M. Hoffmann, N. Pak, G. Wetzstein, S. Kato, T. Schrödel, R. Raskar, M. Zimmer, E.S. Boyden, A. Vaziri, Nature Methods **11**(7), 727 (2014). DOI 10.1038/nmeth.2964
23. H. Li, C. Guo, S. Jia, in *Frontiers in Optics 2017 (2017), paper FW6D.3* (Optical Society of America, 2017), p. FW6D.3. DOI 10.1364/FIO.2017.FW6D.3. URL https://www.osapublishing.org/abstract.cfm?uri=FiO-2017-FW6D.3
24. N.C. Pégard, H.Y. Liu, N. Antipa, M. Gerlock, H. Adesnik, L. Waller, Optica **3**(5), 517 (2016). DOI 10.1364/OPTICA.3.000517. Publisher: Optical Society of America
25. O. Skocek, T. Nöbauer, L. Weilguny, F. Martínez Traub, C.N. Xia, M.I. Molodtsov, A. Grama, M. Yamagata, D. Aharoni, D.D. Cox, P. Golshani, A. Vaziri, Nature Methods **15**(6), 429 (2018). DOI 10.1038/s41592-018-0008-0. Number: 6 Publisher: Nature Publishing Group
26. J. Kim, J.H. Jung, Y. Jeong, K. Hong, B. Lee, Optics Express **22**(9), 10210 (2014). DOI 10.1364/OE.22.010210
27. N.T. Ouellette, H. Xu, E. Bodenschatz, Experiments in Fluids **40**(2), 301 (2006). DOI 10.1007/s00348-005-0068-7. URL https://doi.org/10.1007/s00348-005-0068-7
28. H. Kim, J. Westerweel, G.E. Elsinga, Measurement Science and Technology **24**(2), 024007 (2012). DOI 10.1088/0957-0233/24/2/024007. URL https://doi.org/10.1088/0957-0233/24/2/024007
29. G.E. Elsinga, F. Scarano, B. Wieneke, B.W. van Oudheusden, Experiments in Fluids **41**(6), 933 (2006). DOI 10.1007/s00348-006-0212-z. URL https://doi.org/10.1007/s00348-006-0212-z
30. A. Bajpayee, A.H. Techet, Experiments in Fluids **58**(8), 95 (2017). DOI 10.1007/s00348-017-2373-3. URL https://doi.org/10.1007/s00348-017-2373-3
31. K. Lynch, Development of a 3-d fluid velocimetry technique based on light field imaging. Ph.D. thesis, Auburn University (2011)
32. T.T. Truscott, J. Belden, R. Ni, J. Pendlebury, B. McEwen, Experiments in Fluids **58**, 16 (2017). DOI 10.1007/s00348-016-2297-3. URL https://doi.org/10.1007/s00348-016-2297-3
33. Z. Pan, M. Lu, S. Xia, Experimental Mechanics **59**(5), 713 (2019). DOI 10.1007/s11340-019-00522-2. URL https://doi.org/10.1007/s11340-019-00522-2
34. J.B. Estrada, C. Barajas, D.L. Henann, E. Johnsen, C. Franck, Journal of the Mechanics and Physics of Solids **112**, 291 (2018). DOI 10.1016/j.jmps.2017.12.006
35. H. Zou, J.P. Schmiedeler, W.N. Hardy, Journal of Biomechanics **40**(6), 1183 (2007). DOI 10.1016/j.jbiomech.2006.06.018. URL http://www.sciencedirect.com/science/article/pii/S0021929006002314
36. A.A. Sabet, E. Christoforou, B. Zatlin, G.M. Genin, P.V. Bayly, Journal of Biomechanics **41**(2), 307 (2008). DOI 10.1016/j.jbiomech.2007.09.016. URL https://linkinghub.elsevier.com/retrieve/pii/S0021929007003880
37. H. Schreier, J.J. Orteu, M.A. Sutton, *Image correlation for shape, motion and deformation measurements* (Springer US, 2009)
38. E. Bar-Kochba, J. Toyjanova, E. Andrews, K.S. Kim, C. Franck, Experimental Mechanics **55**(1), 261 (2015). DOI 10.1007/s11340-014-9874-2. URL http://link.springer.com/10.1007/s11340-014-9874-2
39. M. Patel, S.E. Leggett, A.K. Landauer, I.Y. Wong, C. Franck, Scientific Reports **8**(1) (2018). DOI 10.1038/s41598-018-23488-y. URL http://www.nature.com/articles/s41598-018-23488-y
40. L. Hazlett, A.K. Landauer, M. Patel, H.A. Witt, J. Yang, J.S. Reichner, C. Franck, Scientific reports **10**(1), 1 (2020)
41. J. Yang, Y. Yin, A.K. Landauer, S. Buyuktozturk, J. Zhang, L. Summey, A. McGhee, M.K. Fu, J.O. Dabiri, C. Franck. Serialtrack: Scale and rotation invariant augmented lagrangian particle tracking (2022). DOI 10.48550/ARXIV.2203.12573. URL https://arxiv.org/abs/2203.12573
42. M.T. Scimone, H.C. Cramer Iii, E. Bar-Kochba, R. Amezcua, J.B. Estrada, C. Franck, Nature Protocols **13**(12), 3042 (2018). DOI 10.1038/s41596-018-0077-7. URL https://www.nature.com/articles/s41596-018-0077-7
43. A. Stefanoiu, J. Page, P. Symvoulidis, G.G. Westmeyer, T. Lasser, Optics Express **27**(22), 31644 (2019). DOI 10.1364/OE.27.031644
44. T. Georgiev, C. Intwala, Adobe Technical Report (2006)
45. L. Adrian, R.J. Adrian, J. Westerweel, *Particle image velocimetry*. 30 (Cambridge university press, 2011)
46. S.G. Knoll, M.Y. Ali, M.T.A. Saif, Journal of Visualized Experiments : JoVE p. 51873 (2014). DOI 10.3791/51873
47. L. Summey, Master's thesis, University of Wisconsin - Madison, Madison, Wisconsin (2020)
48. K. Hyun, M. Wilhelm, C.O. Klein, K.S. Cho, J.G. Nam, K.H. Ahn, S.J. Lee, R.H. Ewoldt, G.H. McKinley, Progress in Polymer Science **36**(12), 1697 (2011). DOI 10.1016/j.progpolymsci.2011.02.002
49. S. Buyukozturk, A.K. Landauer, J. Zhang, L. Summey, C. Angel, C. Franck. High-speed, 3d volumetric displacement and strain mapping in soft materials using light field microscopy [data set] (2022). DOI https://doi.org/10.21231/YQZY-7X90
50. S.L. Liu, J. Li, Z.L. Zhang, Z.G. Wang, Z.Q. Tian, G.P. Wang, D.W. Pang, Scientific Reports **3**(1), 2462 (2013). DOI 10.1038/srep02462. URL https://www.nature.com/articles/srep02462
51. T. Janke, R. Schwarze, K. Bauer, SoftwareX **11**, 100413 (2020). DOI 10.1016/j.softx.2020.100413
52. A.K. Landauer, M. Patel, D.L. Henann, C. Franck, Experimental Mechanics **58**(5), 815 (2018). DOI 10.1007/s11340-018-0377-4